Measurement of smoothed Wigner phase-space distributions for small-angle scattering in a turbid medium

A. Wax and J. E. Thomas

Department of Physics, Duke University, Durham, North Carolina 27708-0305

Received October 15, 1997; revised manuscript received January 16, 1998; accepted February 4, 1998

We study Wigner phase-space distributions $W(x, p)$ in position (x) and momentum (p) for light undergoing multiple small-angle scattering in a turbid medium. Smoothed Wigner phase-space distributions are measured by using a heterodyne technique that achieves position and momentum resolution determined by the width and the diffraction angle of the local oscillator beam. The sample consists of 5.7-μm-radius polystyrene spheres suspended in a water–glycerol mixture. The momentum distribution of the transmitted light is found to contain a ballistic peak, a narrow diffractive pedestal, and a broad background. The narrow diffractive pedestal is found to decay more slowly than the ballistic peak as the concentration of scatterers is increased. The data are in excellent agreement with a simple theoretical model that explains the behavior of the narrow pedestal by including multiple diffractive scattering and treating large-angle scattering as a loss. © 1998 Optical Society of America [S0740-3232(98)00907-7]

OCIS codes: 110.7050, 170.1650, 290.4210, 290.5820, 040.2840.

1. INTRODUCTION

Propagation of optical coherence in multiple-scattering media is currently receiving renewed attention because of its importance in the development of new biological and medical imaging methods based on optical fields.[1] It has been suggested by Raymer and co-workers and independently by John *et al.* that new venues for medical imaging may be based on coherence tomography employing measurement of Wigner phase-space distributions in multiple-scattering media.[2–4] Wigner distributions yield information about the optical amplitude and phase in terms of the joint position and momentum phase-space distribution of the optical field.

In 1932 Wigner[5] introduced a wave-mechanical phase-space distribution function that is applicable to coherence tomography. This distribution plays a role closely analogous to that of a classical phase-space distribution in position and momentum. For a wave field varying in one spatial dimension, $\mathscr{E}(x)$, the Wigner phase-space distribution is given by[6]

$$W(x, p) = \int \frac{d\epsilon}{2\pi} \exp(i\epsilon p)\langle \mathscr{E}^*(x + \epsilon/2)\mathscr{E}(x - \epsilon/2)\rangle, \tag{1}$$

where x is the position, p is a wave vector (momentum), and $\langle\cdot\rangle$ denotes a statistical average. It is easy to show that $\int dp\ W(x, p) = \langle|\mathscr{E}(x)|^2\rangle$, the position distribution of the intensity, and $\int dx\ W(x, p) = \langle|\mathscr{E}(p)|^2\rangle$, the corresponding momentum distribution. These results suggest that $W(x, p)$ is analogous to a classical phase-space distribution in x and p. However, Eq. (1) shows that the Wigner distribution is Fourier transform related to the two-point mutual coherence function and therefore is sensitive to the spatially varying phase and amplitude of the field.

Wigner phase-space distributions obey rigorous transport equations, which are derivable from the underlying optical wave equations. Thus measurement methods based on Wigner distributions can be placed on a firm theoretical footing and permit detailed study of the propagation of optical coherence in multiple-scattering media for comparison with theory. Hence studies of Wigner distributions will impact many current imaging methods, such as optical coherence tomography (OCT)[7,8] and optical coherence microscopy (OCM).[9]

Certain features of Wigner distributions have been predicted to propagate coherently over distances large compared with the transport mean free path in multiple-scattering media,[4] permitting measurements through thick samples. Further, coherence tomography based on measurement of Wigner phase-space distributions may provide very-high-resolution imaging, as Wigner distributions contain information on an optical wavelength scale: according to Eq. (1), the two-point spatial coherence function and the Wigner function are Fourier transform related. Hence the spatial resolution in determining spatial correlations is inversely proportional to the range of momenta that is measured. For measurements that are carried out for an angular region of a substantial fraction of a radian, spatial correlations are resolved at the level of a few optical wavelengths.

A unique feature of Wigner phase-space distributions is that they bridge the gap between phenomenological transport equations, on which the diffusion approximation is based, and rigorous wave equation treatments.[10] In particular, the Wigner distribution is the rigorous wave-field analog of the phenomenological specific intensity. The Wigner distribution includes statistically averaged coherent and incoherent contributions to the transmitted or reflected light and rigorously incorporates

0740-3232/98/071896-13$15.00

phase and intensity information. Therefore measurement and study of such distributions is likely to lead to new insights into the nature of light propagation in multiple-scattering media and hence to new avenues for sensitive, high-resolution biological imaging.

Despite their frequent use in theory[11] and potential practical importance to tomographic imaging, Wigner phase-space distributions have received relatively little attention in optical measurements. It has been shown that Wigner distributions for optical fields can be determined by tomographic inversion of intensity measurements obtained in a number of planes.[3] The Wigner distribution can also be obtained by Fourier transformation of the two-point coherence function measured by shearing interferometry.[2] Measurement of two-point coherence functions by this method has been suggested and demonstrated previously.[12]

Recently, we have developed a sensitive heterodyne method for measuring smoothed Wigner phase-space distributions with the use of a simple optical system.[13] The spatial width and the diffraction angle of the local oscillator (LO) beam determine the position and momentum resolution with which the smoothed Wigner function is measured. Very high dynamic range has been achieved: 13 orders of magnitude (130 dB) has been demonstrated in our laboratory by using milliwatt cw lasers.[14]

As described below, in the heterodyne method, the Wigner distribution of the transmitted light is smoothed by convolution with the Wigner distribution of the LO beam. In principle, a smoothed Wigner distribution can be obtained by using pinholes, one near the source to determine the position and a second pinhole, widely separated from the first, to determine the momentum. In this case the Wigner function of the transmitted light is smoothed by convolution with the Wigner function for the two separated pinholes. For the heterodyne method, the Wigner function for the LO is Gaussian in momentum and position, yielding a minimum uncertainty product. However, the position and momentum resolution cannot be varied independently in either case. The smoothed Wigner distribution is therefore coarse grained and contains less information on the phase and the amplitude of the field than the true Wigner distribution of the transmitted light. As noted above, the latter can be determined from the two-point coherence function measured by shearing interferometry, where the position and momentum resolution can be independently controlled.[2] Nevertheless, as shown below, the heterodyne method provides a simple means of obtaining smoothed Wigner distributions directly as phase-space contour plots. In many cases of practical interest, this method can provide substantial sensitivity to both the coherence and the intensity of the light transmitted through biological materials.

Smoothed Wigner distributions are obtained in our experiments as mean square heterodyne beat signals. Mean square beat signals are sensitive both to ballistically transmitted light and to light that has been multiply scattered into the mode of the LO.[14] By contrast, in OCT the mean heterodyne beat signal is measured to suppress all scattered light. The difference between mean and mean square beat signals has been discussed previously for homodyne detection.[15]

To exploit fully the information about the form factor of the scattering object that is contained in the Wigner distribution, it is necessary to suppress unwanted contributions arising from diffuse scattering as much as possible. Compared with methods that measure only the position-dependent intensity, measurement of smoothed Wigner distributions with high angular resolution suppresses the contribution of diffuse scatter, which has a broad angular distribution. In addition, the heterodyne technique permits phase-space distributions to be measured with the use of either coherent or low-coherence-length light sources, allowing additional suppression of diffuse scatter.[16] Heterodyne measurement can be used to measure smoothed Wigner distributions for low-order scattered light that retains substantial information about the scatterer without suffering as much attenuation as the ballistic light. Thus this method will complement current studies of low-order light scattering.[17,18]

In this paper we describe measurements of smoothed Wigner phase-space distributions for multiple small-angle scattering in a medium consisting of 5.7-μm-radius polystyrene spheres suspended in a water-glycerol mixture. Our experiments use a helium–neon (He–Ne) laser as a coherent light source and will serve as a basis for comparison with future work employing low-coherence light sources to measure smoothed Wigner phase-space distributions for low-order scattered light in the same medium.

Measurements of smoothed Wigner distributions for small-angle scattering are relevant to OCT and OCM, since it has been shown recently that multiple small-angle scattering increases the effective probe field over that expected for simple exponential decay of the ballistic light. The probe field contains a distorted wave front that causes structures that are small compared with the transverse coherence length of the unscattered input beam to be enhanced in comparison with large ones.[19]

The remainder of this paper is organized as follows. The heterodyne method for measuring smoothed Wigner phase-space distributions as contour maps is described in Section 2. This method is used to measure the smoothed Wigner phase-space distribution for light transmitted through a sample of polystyrene spheres suspended in a water–glycerol mixture. It is demonstrated that the smoothed Wigner phase-space contours are sensitive to both the coarse-grained intensity and the wave-front curvature of the emerging light. A narrow pedestal is observed in the phase-space contour and is explored in substantial detail in Section 3. An analysis is carried out in the language of Wigner distributions, showing that the narrow pedestal arises from multiple diffractive scattering. The experimental measurements are in excellent agreement with a simple model that treats large-angle scattering as a loss. These results are related to previous analyses of small-angle scattering.

2. EXPERIMENT

We have developed a simple optical heterodyne technique for directly measuring smoothed Wigner phase-space dis-

tributions as phase-space contour plots with high dynamic range. Spatial and momentum resolutions are determined by the spatial width and diffraction angle of the LO beam. In this case the smoothed Wigner distributions that are obtained are always positive definite.[20] This method is well suited for measuring small-angle scattering distributions with high angular resolution. We apply this technique to measure smoothed Wigner phase-space contours for light transmitted through a turbid medium.

A. Scheme

The scheme of the heterodyne experiments, shown in Fig. 1, employs a He–Ne laser beam, which is split into a 1-mW LO beam and a 1-mW input beam to the sample. The relative frequency between the LO and the input beam is determined by acousto-optic modulators that differ in drive frequency by 10 MHz. The transmitted beam from the sample (signal beam) is mixed with the LO at a 50–50 beam splitter (BS2). Technical noise is suppressed by employing a standard balanced detection system.[21] The beat signal at 10 MHz is measured with an analog spectrum analyzer. An important feature of the experiments is that the analog output of the spectrum analyzer is squared by using a low-noise multiplier.[22] The multiplier output is fed to a lock-in amplifier, which subtracts the mean square signal and noise voltages with the input beam on and off.[23] In this way the mean square electronic noise and the LO shot noise are subtracted in real time, and the lock-in output is directly proportional to the mean square beat amplitude $|V_B|^2$. The mean square beat signal is directly proportional to the overlap of the Wigner phase-space distributions for the LO and signal fields,[13] as shown briefly below.

The beat amplitude V_B is determined in the paraxial ray approximation by the spatial overlap of the LO and signal (denoted by subscript S) fields in the plane of the detector, $z = z_D$.[24] Using Fourier optics, we can relate the fields in the detector plane (D1, D2) to the fields in the source planes ($z = 0$) of the input achromatic lenses L1 and L2, which have equal focal lengths $f = 6$ cm. When the input lens L2 is translated off axis by a distance d_p and the mirror M1 is translated off axis by a distance d_x, the mean square beat amplitude for a narrow-band field takes the simple form

$$|V_B|^2 \propto \left| \int dx' \, \mathscr{E}^*_{\mathrm{LO}}(x', z_D)\mathscr{E}_S(x', z_D) \right|^2$$
$$\propto \left| \int dx \, \mathscr{E}^*_{\mathrm{LO}}(x - d_x, z = 0) \times \mathscr{E}_S(x, z = 0)\exp\left(ik_o \frac{d_p}{f} x \right) \right|^2 . \quad (2)$$

Here x' denotes position in the detector plane, x denotes position in the source plane, $\mathscr{E}$ is a slowly varying field amplitude (band center frequency phase factor removed), and $k_o = 2\pi/\lambda_o$ is the wave vector in air. For simplicity, the corresponding y integrals are suppressed, as is the statistical average. It is assumed that the Rayleigh and coherence lengths of the LO and signal fields are large compared with d_x, so that the translation of M1 simply shifts the center of the input LO field without significantly altering the LO optical path length before L1. When this is not the case, a translating corner cube can be added to the LO arm to compensate for path-length changes arising from M1. The detectors are located in the Fourier plane $z_D = f$ of the lenses L1 and L2, so that the LO position in the detector plane remains fixed as d_x is scanned.

Using Eq. (1), we can rewrite relation (2) (suppressing the y integration) as

$$|V_B(d_x, d_p)|^2 \propto \int dx dp \; W_{\mathrm{LO}}(x - d_x, p + k_o d_p/f) W_S(x, p), \quad (3)$$

where $W_S(x, p)$ is the Wigner distribution of the signal field in the plane of L2 ($z = 0$), given by Eq. (1). $W_{\mathrm{LO}}(x, p)$ is the LO Wigner distribution in the plane of L1.

From relation (3) we see that the mean square beat signal is the convolution integral of the LO and signal field Wigner phase-space distributions. Hence the mean square beat signal that is obtained in real time in the experiments is a smoothed Wigner distribution.[20] Scanning the positions of M1 by d_x and L2 by d_p with the use of stepper translators yields a contour map of W_S with resolution limited by the phase-space resolution of the LO. This method permits position measurement over a range of ± 1 cm and momentum measurement over a range of ± 300 mrad. With the definitions $x_M = d_x$ and $p_M = -k_o d_p/f$, the mean square beat signal S can be rewritten as

$$S(\mathbf{x}_{M\perp}, \mathbf{p}_{M\perp}) = \int d^2\mathbf{x}_\perp d^2\mathbf{p}_\perp \; W_{\mathrm{LO}}(\mathbf{x}_\perp - \mathbf{x}_{M\perp}, \mathbf{p}_\perp - \mathbf{p}_{M\perp}) W_S(\mathbf{x}_\perp, \mathbf{p}_\perp). \quad (4)$$

Here the subscript $\perp$ denotes the direction perpendicular to the z axis. The transverse Wigner distribution at the exit of the sample ($z = L$) is given in terms of the three-dimensional Wigner distribution by

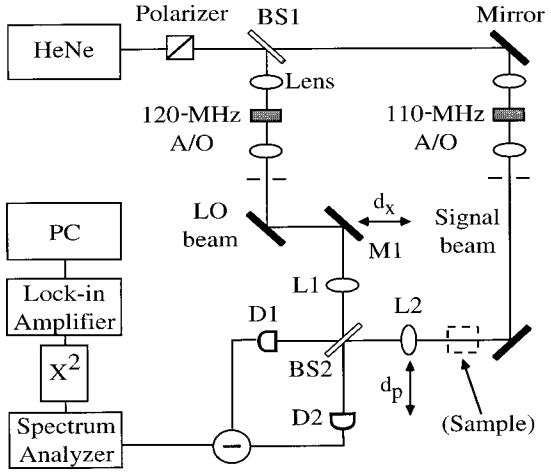

Fig. 1. Heterodyne measurement of smoothed Wigner phase-space distributions.

$$W_S(\mathbf{x}_\perp, \mathbf{p}_\perp) = \int \mathrm{d}p_z \, W_S(z = L, \mathbf{x}_\perp, \mathbf{p}). \tag{5}$$

Analogous to Eq. (1), the three-dimensional Wigner distribution is defined by

$$W(\mathbf{x}, \mathbf{p}, t) = \int \frac{\mathrm{d}^3\epsilon}{(2\pi)^3} \exp(i\epsilon \cdot \mathbf{p}) \mathscr{E}^*(\mathbf{x} + \epsilon/2, t) \times \mathscr{E}(\mathbf{x} - \epsilon/2, t), \tag{6}$$

where $\mathbf{x}$ denotes position and $\mathbf{p}$ is a wave vector (momentum).

The transverse Wigner distributions that appear in Eq. (4) have an important property. Since the transverse momentum $\mathbf{p}_\perp$ is conserved in propagation between media of different indices of refraction, the transverse Wigner distribution does not change in propagating between the sample and the air. This is a consequence of the boundary condition that yields Snell's law: the momentum in the plane of the interface is conserved, although the magnitude of the total momentum vector changes. Hence the angles of incidence and refraction must be different.

As a simple demonstration of the physical content of Eq. (4), we have measured smoothed Wigner distributions for Gaussian beams with curvature and for a source consisting of two mutually coherent Gaussian beams.[13] These measurements show how the Wigner distribution is sensitive to the coarse-grained spatially varying phase and amplitude of the field in the source plane of lens L2.

B. Smoothed Wigner Distribution for Light Transmitted through a Turbid Medium

We have measured the smoothed Wigner distribution for the field transmitted through a turbid medium consisting of latex microspheres ($n = 1.59$) in a mixture of 25% glycerol and 75% water. This mixture is chosen to produce neutral buoyancy for the microspheres. The index of refraction of the mixture is found to be 1.36 by passing a He–Ne laser beam through a triangular container similar to an equilateral triangular prism. By noting the angular deviation, we are able to measure the index of refraction to be within 0.3% of published values for this mixture at this wavelength. This index of refraction for the medium results in a relative refractive index of 1.17 for the latex microspheres compared with the medium.

Large spheres are specifically selected to give highly forward-peaked scattering. The spheres used in this experiment have a radius of 5.7 μm. The Mie solution[25] for the above parameters gives a total scattering cross section σ_S that is 1.98 times the geometrical cross section, i.e., $\sigma_S = 202\ \mu\mathrm{m}^2$. It is assumed that there is no absorption. The theoretical angular distribution (differential cross section) is shown in Fig. 2. The peak amplitude has been normalized to 1. The angles are the transverse momenta given in units of the photon wave vector k_o in vacuum. These angles have been multiplied by 1.36 to account for the propagation from the water–glycerol mixture into air, where they are detected. The differential scattering cross section shows a central diffractive peak that is nominally Gaussian. Its half-width at $1/e$ is 31.6 mrad, which corresponds to a width of 23.2 mrad in the medium. This distribution is highly peaked in the forward direction, with a low-amplitude broad background that is not visible here. Data were taken for varying concentrations of spheres in water–glycerol in a precision cell of optical path length $L = 10$ mm.

Initially, we have measured the smoothed Wigner distribution for transmission of a narrow, collimated Gaussian beam through this sample. Figure 3 shows a measured phase-space contour plot (log scale) for a 0.5-mm-diameter input beam to the sample. Here the concentration of 5.7-μm-radius spheres is $\rho = 2 \times 10^6/\mathrm{cm}^3$, and the ballistic contribution is attenuated by $\exp(-4)$. The ballistic light appears as a narrow island in the center of the contour plot. A narrow pedestal appears around the ballistic contribution. Both the pedestal and the broad large-angle scattering contribution exhibit a correlation between momentum and position, as expected for a diverging localized source. This corresponds to a wave-front curvature of 2.1 cm, approximately the distance between the input face of the sample and the input plane (center) of lens L2, where the signal Wigner

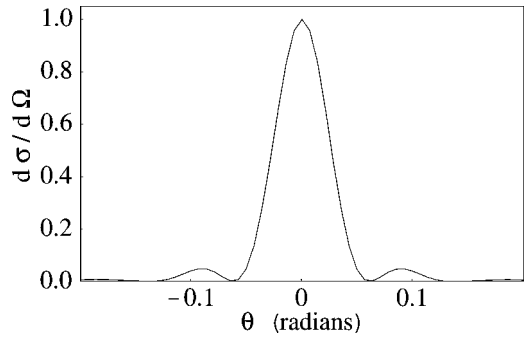

Fig. 2. Mie differential cross section for scattering from 11.4-μm polystyrene spheres, with parameters $n_{\mathrm{rel}} = 1.17$, $n_o = 1.36$, and $\lambda_{\mathrm{air}} = 633$ nm.

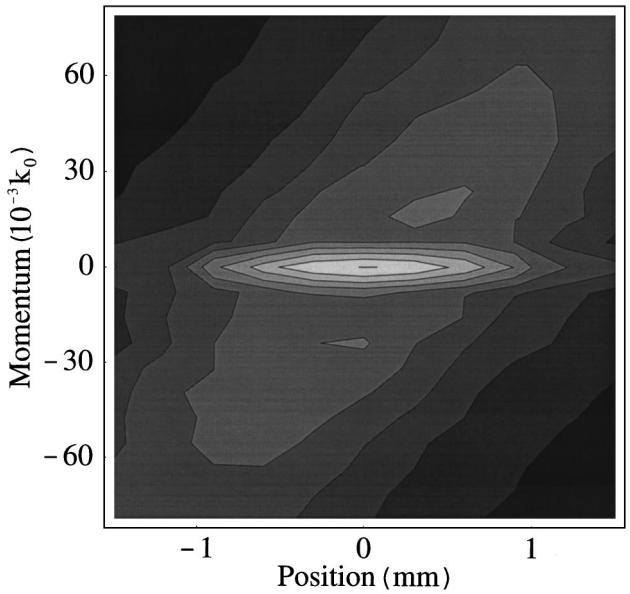

Fig. 3. Smoothed Wigner distribution (log scale) for light transmitted though a turbid medium for $\rho = 2 \times 10^6/\mathrm{cm}^3$. x denotes the transverse position in millimeters, and p denotes the transverse wave vector (momentum) in units of the wave vector in air, k_o. The central island is the ballistic contribution.

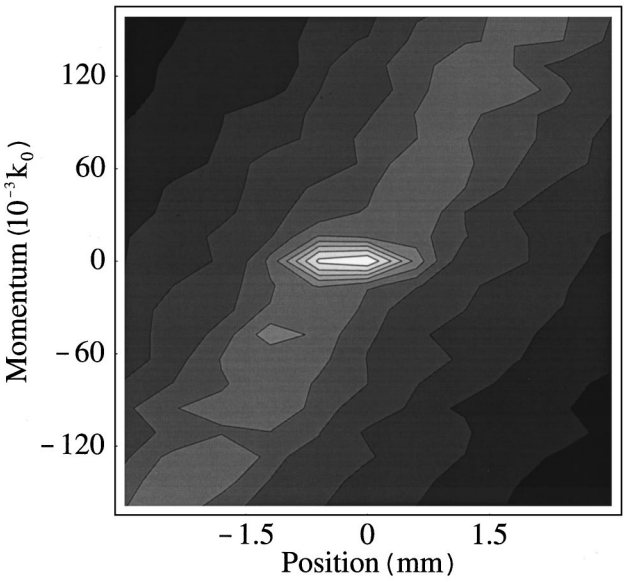

Fig. 4. Smoothed Wigner distribution (log scale) for $\rho = 6 \times 10^6/\text{cm}^3$. The central island is the ballistic contribution. Note the appearance of a narrow pedestal centered on the ballistic feature.

distribution is sampled. Figure 4 shows the phase-space contours at a higher concentration, $\rho = 6 \times 10^6/\text{cm}^3$, where the ballistic attenuation is $\exp(-12)$. In this case the momentum and position distributions broaden. (Note the increased horizontal and vertical scales.) The correlation between position and momentum indicates a wave-front curvature of 1.5 cm, corresponding to a source located near the center of the cell. At higher concentrations the source position appears to move toward the sample output face. From the width of the momentum distribution at $x = 0$, the transverse coherence length for the multiply scattered light is estimated to be approximately 2 μm.

C. Wigner Distribution for Small-Angle Scattered Light

To explore in detail the shape and the amplitude of the pedestal shown in Fig. 3, we have measured the smoothed Wigner distributions for transmission of a large-diameter input beam through the sample ($a = 3.8$ mm half-width at 1/e intensity). In this case the LO beam is small in diameter ($a_o = 0.38$ mm) compared with the input beam, so that the output Wigner distribution is nearly independent of position x over the LO diameter. Further, the momentum width of the LO is small compared with the width of the momentum distribution of the scattered light. In this case the measured mean square heterodyne beat signal $S(x_M = 0, p_M)$ determines approximately the true transmitted Wigner distribution of the scattered light, $W_S(x = 0, p_M)$, excluding the ballistic contribution that is sharply peaked in the forward-scattering direction [see Eq. (15) below].

For fixed LO position $x_M = 0$, plots of $S(x_M = 0, p_M) = W_S(x = 0, p_M)$ are shown for various concentrations of 5.7-μm-radius spheres ranging from $\rho = 0.4 \times 10^6/\text{cm}^3$ to $\rho = 6 \times 10^6/\text{cm}^3$. In general, the scattering distribution is seen to have three components: a ballistic peak, a central narrow pedestal, and a broad diffuse background. The ballistic contribution is not shown, as it is orders of magnitude larger than the narrow pedestal and the diffuse background. The half-width at 1/e intensity of the ballistic peak is 0.4 mrad, which is much narrower than the widths of the scattered-light distributions. At low concentrations the scattered-light data show a diffractive peak (Fig. 5), which agrees with the Mie solution. As the concentration is increased (Fig. 6), the diffractive peak is seen to broaden and attenuate while the broad background becomes more prominent, until in Fig. 7 the diffuse background becomes comparable with the diffractive component. Here the ballistic component is still a factor of 10 larger than the pedestal and is not shown.

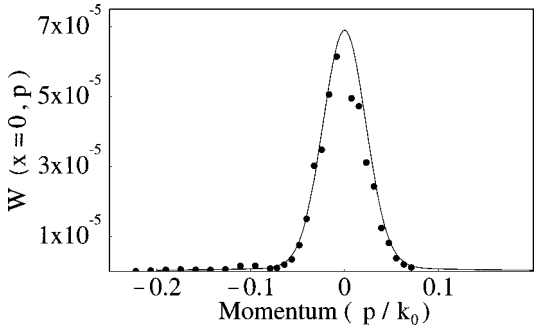

Fig. 5. Smoothed Wigner distribution $\simeq W(x = 0, p)$ (linear scale, ballistic contribution not shown) for $\rho = 0.4 \times 10^6/\text{cm}^3$. Note that here the input beam is large compared with the diameter of the LO beam. The theoretical prediction is shown as a solid curve.

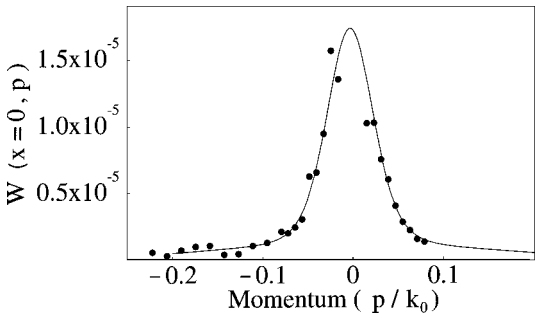

Fig. 6. Smoothed Wigner distribution $\simeq W(x = 0, p)$ for large input beam (linear scale, ballistic contribution not shown) for $\rho = 2 \times 10^6/\text{cm}^3$. Note the narrow central pedestal arising from diffractive scattering. The solid curve shows the theoretical prediction.

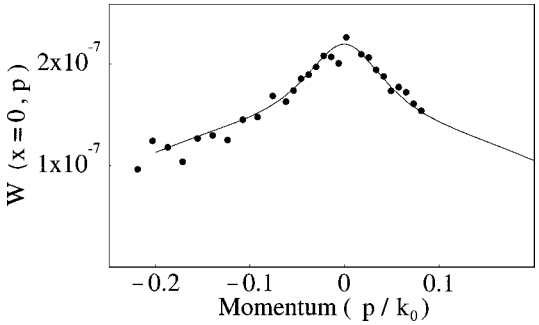

Fig. 7. Smoothed Wigner distribution $\simeq W(x = 0, p)$ (linear scale, ballistic contribution not shown) for $\rho = 6 \times 10^6/\text{cm}^3$. Note the increase in the narrow central pedestal arising from diffractive scattering. The solid curve shows the theoretical prediction.

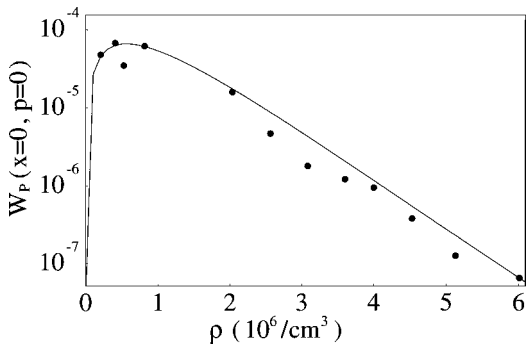

Fig. 8. Amplitude of the narrow pedestal arising from multiple diffractive scattering as a function of scatterer concentration ρ. The solid curve shows the prediction with no free parameters. Note that the amplitude of the pedestal decays with an extinction coefficient that is 0.65 of the ballistic extinction coefficient of Fig. 9.

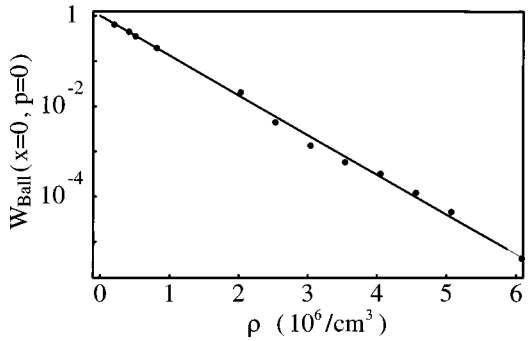

Fig. 9. Amplitude of the ballistic component as a function of scatterer concentration ρ. The solid line shows the prediction for exponential decay with the extinction coefficient determined from the total scattering cross section.

The experimental angular distributions $W_S(x = 0, p)$ are fitted to two-component curves (solid curves) consisting of a narrow central pedestal and a broad diffuse background. As discussed above, the ballistic contribution is ignored, as it is localized near the origin. The central pedestal in the two-component curve arises from multiple diffractive scattering. The shape of this component (normalized to 1 at $p = 0$) is determined by using the theory described in detail in Section 3. The amplitude of this component is left as a free parameter and is compared below with the predicted value. The broad background, which is not of interest here, is modeled as a Gaussian distribution in p with an undetermined amplitude.

Figure 5 shows the angular scattering distribution $W_S(x = 0, p)$ for a scatterer concentration of $\rho = 0.4 \times 10^6/\text{cm}^3$. The transverse momentum p is given in units of the optical wave vector in air, k_o. The position x is in millimeters. This figure shows data points that are taken for angles $\theta = p/k$ in the range from -225 to $+75$ mrad. However, the fitted curve (solid curve) is done for the data outside ± 30 mrad, as interference with the Gaussian tail of the ballistic light distribution causes these points to be unreliable. The ballistic peak is attenuated at this concentration by $\exp(-0.8)$ and is not shown in this figure, as it is orders of magnitude larger than the scattered light.

Figure 6 shows the angular scattering distribution at a higher concentration, $\rho = 2 \times 10^6/\text{cm}^3$. Here we can see the broad diffuse background become significant, whereas the central pedestal has broadened slightly. The ballistic light at this concentration has been attenuated by $\exp(-4)$ and again is not shown here, as it is orders of magnitude larger than the scattered intensity.

In Fig. 7 the angular scattering distribution is shown for a scatterer concentration $\rho = 6 \times 10^6/\text{cm}^3$. In this plot we see that the broad background has become comparable in magnitude with the central pedestal. At this concentration the ballistic light has been attenuated by $\exp(-12)$, 1 order of magnitude larger than the scattered light, so again it is not shown.

To explore how the amplitude of the central pedestal varies with concentration, the maximum amplitudes for each of the fitted curves are shown in Fig. 8 as a function of scatterer concentration. These are compared with the predicted amplitude (solid curve) with no free parameters. For comparison, the amplitude of the ballistic peak as a function of scatterer concentration is shown in Fig. 9. Over most of the range of scatterer concentrations, the amplitude of the central pedestal (Fig. 8) is found to decay exponentially with an attenuation coefficient that is 65% of that found for the ballistic extinction coefficient.

3. THEORY

The data obtained in the experiments exhibit a number of interesting features that can be understood in terms of a simple model for multiple diffractive scattering. In this model multiple diffractive scattering is included by means of a collision integral, but large-angle scattering is treated as a loss. In addition, the input beam is assumed large in diameter compared with the LO beam, so that the system exhibits approximate translation invariance across the output face of the sample.[26] These conditions are approximately satisfied in the experiments.

In general, the transport equation for the Wigner distribution can be somewhat complicated, exhibiting nonlocal scattering.[4,27] However, when the Wigner distribution varies slowly in its spatial argument compared with an optical wavelength, the transport equation is approximately local and is identical in structure to the usual radiative transport equation for the specific intensity.[4,27] Hence, as a first approximation, we use this equation to model our data. For cw narrow-band excitation, the Wigner distribution is time independent and obeys the following approximate transport equation:

$$\frac{c^2\mathbf{p}}{{n_o}^2\omega} \cdot \nabla_x W(\mathbf{x}, \mathbf{p}) = -\frac{c}{n_o}\mu_T(\mathbf{p})W(\mathbf{x}, \mathbf{p}) + \int \mathrm{d}^3\mathbf{p}'\, K(\mathbf{p}, \mathbf{p}')W(\mathbf{x}, \mathbf{p}'). \tag{7}$$

Here the vector properties of the field are neglected. n_o is the mean index of refraction of the background medium, c/n_o is the speed of light in the medium, $\mathbf{p}$ is a wave vector of magnitude $p = k \equiv n_o k_o$, with $k_o = \omega/c$, and ω is the optical frequency. The extinction coefficient arising from the total scattering cross section (and absorp-

tion) is $\mu_T(\mathbf{p})$. The total loss rate of optical phase-space density for wave vector $\mathbf{p}$ is $(c/n_o)\mu_T(\mathbf{p})$. The collision kernel (phase function) $K(\mathbf{p}, \mathbf{p}')$ is the arrival rate of phase-space density from wave vector $\mathbf{p}'$ to $\mathbf{p}$.

A. Two-Component Kernel

For Mie scattering from 11.4-μm spheres, the differential scattering cross section (Fig. 2) exhibits a large diffractive scattering component that is forward peaked. In addition, there is a component that scatters broadly into 4π solid angle. This corresponds approximately to the geometrical (classical) scattering cross section. According to the Mie differential scattering cross section, approximately 65% of the total scattering cross section arises from the broad part and 35% from the diffractive part. In this case the kernel can be modeled as having two distinct components, denoted as K_N and K_B, respectively, where N denotes the narrow diffractive kernel and B the broad kernel:

$$K(\mathbf{p}, \mathbf{p}') = K_N(\mathbf{p}, \mathbf{p}') + K_B(\mathbf{p}, \mathbf{p}'). \tag{8}$$

It is convenient to divide the Wigner phase-space distribution into three components:

$$W = W_{\mathrm{BALL}} + W_P + W_B. \tag{9}$$

Here W_{BALL} denotes the narrow contribution arising from purely ballistic propagation of the input phase-space distribution with attenuation at the total loss rate, W_P denotes the phase-space distribution of the narrow pedestal that arises from diffractive scattering, and W_B denotes a broad background contribution arising from large-angle scattering.

As shown in Appendix A, an evolution equation can be derived for each of the components of the Wigner distribution. The derivation is closely related to those employed in previous studies of small-angle scattering.[28]

The phase-space distribution for the ballistic pedestal obtained by solving Eq. (A6) is given by

$$W_{\mathrm{BALL}}(z, \mathbf{x}_\perp; \mathbf{p}) \simeq \exp(-\mu_T z) W^0_{\mathrm{BALL}}(z = 0, \mathbf{x}_\perp - z\mathbf{p}_\perp/k; \mathbf{p}). \tag{10}$$

Here we have assumed that the input beam is a collimated Gaussian laser beam with a half-width at $1/e$ intensity of a and that $p_z \simeq k$ and $v_z \simeq c/n_o$. The input distribution just inside the medium at $z = 0$ is given by

$$W^0_{\mathrm{BALL}}(z = 0, \mathbf{x}_\perp; \mathbf{p}) \simeq \delta(p_z - k)\,\frac{1}{\pi^2}\exp\left[-\frac{x^2 + y^2}{a^2} - a^2(p_x^2 + p_y^2)\right]. \tag{11}$$

Note that W^0_{BALL} is normalized so that $\int d^2\mathbf{x}_\perp d^3\mathbf{p}\, W^0_{\mathrm{BALL}}(\mathbf{x}, \mathbf{p}) = 1$. The total extinction coefficient $\mu_T = \rho\sigma_T$ arises from the total scattering cross section and absorption.

An important feature of relation (10) is that it appears to describe classical linear trajectories for the optical intensity. Nevertheless, the Wigner distribution obtained by using relation (11) correctly describes diffraction, as is readily shown by integration of relation (10) over p_x and p_y.[13]

The Wigner distribution W_P for the pedestal is obtained by using the approximate kernel of relation (A10) as described in Appendix A. W_P is given by Eq. (A23):

$$W_P(L, \mathbf{x}_\perp; \mathbf{p}) = \delta(p_z - k) W_P(L, \mathbf{x}_\perp, \mathbf{p}_\perp). \tag{12}$$

The transverse Wigner distribution for the pedestal is given by Eq. (A26):

$$W_P(L, \mathbf{x}_\perp, \mathbf{p}_\perp) = \frac{\exp(-x_\perp^2/a^2)}{\pi^2\theta_o^2 k^2 a^2}\exp(-\mu_T L) \times \int_0^\infty d\eta_\perp\, 2\eta_\perp J_0\left(\eta_\perp \frac{2p_\perp}{\theta_o k}\right) \times \{\exp[\mu_N L \exp(-\eta_\perp^2)] - 1\}. \tag{13}$$

Here the magnitude of the transverse momentum is denoted by $p_\perp = |\mathbf{p}_\perp| = \sqrt{p_x^2 + p_y^2}$. Similarly, the magnitude of the transverse position is $x_\perp = |\mathbf{x}_\perp| = \sqrt{x^2 + y^2}$. The scattering diffraction angle obtained from the Mie solution is $\theta_o = 23.2$ mrad. The extinction coefficient $\mu_N = 0.35\mu_S$ arises from diffractive scattering only, where $\mu_S = \rho\sigma_S$ is the extinction coefficient corresponding to the total scattering cross section, i.e., the ballistic extinction coefficient excluding absorption.

B. Mean Square Beat Signal

Equation (4) gives the measured mean square beat signal in terms of the transverse Wigner distributions for the LO and signal fields. With the LO displaced in position and momentum along the $\mathbf{x}$ axis only, the transverse Wigner distribution for the LO field is given by

$$W_{\mathrm{LO}}(\mathbf{x}_\perp - \mathbf{x}_{M\perp}, \mathbf{p}_\perp - \mathbf{p}_{M\perp}) = \frac{1}{\pi^2}\exp\left[-\frac{(x - x_M)^2 + y^2}{a_o^2}\right] \times \exp\{-a_o^2[(p_x - p_M)^2 + p_y^2]\}. \tag{14}$$

Our experiments are carried out by using a LO half-width at $1/e$ intensity, a_o, that is small compared with the spatial extent of the signal field, so that $a_o \ll a$. Further, the diffraction angle of the LO is small compared with the scattering diffraction angle: $2/(ka_o) \ll \theta_o$. In this case the Wigner distribution of the LO is sharply peaked in both position and momentum compared with that of the scattered signal field. Since the LO Wigner distribution of Eq. (14) is normalized to 1, the mean square beat signal for the pedestal can be evaluated by using Eq. (4), with Eq. (14) given by the approximation

$$W_{\mathrm{LO}}(\mathbf{x}_\perp - \mathbf{x}_{M\perp}, \mathbf{p}_\perp - \mathbf{p}_{M\perp}) \simeq \delta(x - x_M)\delta(y) \times \delta(p_x - p_M)\delta(p_y).$$

Hence we obtain

$$S_P(x_M, p_M) = W_P(L, x = x_M, y = 0; p_x = p_M, p_y = 0), \tag{15}$$

where we take $p_\perp = \sqrt{p_x^2 + p_y^2} = |p_M|$ in the transverse Wigner distribution for the pedestal, W_P.

As a reference level, the ballistic contribution to the mean square beat signal is determined by using Eq. (14) and relations (10) and (11) in Eq. (4):

$$S_{\mathrm{BALL}}(x_M, p_M) = \frac{{a_o}^2}{\pi^2 a^2} \exp\left(-{a_o}^2 {p_M}^2 - \frac{{x_M}^2}{a^2} \right) \times \exp(-\mu_T L). \quad (16)$$

Diffraction of the input beam is negligible in the experiments and is therefore not included in Eq. (16).

Figures 5–7 show measured smoothed Wigner phase-space distributions that are plotted as the mean square beat signal divided by the maximum ballistic mean square beat signal (for $\rho = 0$ at $x = p = 0$). The latter is given by

$$S_{\mathrm{MBALL}} = \eta_{\mathrm{het}}^2 ({a_o}^2/\pi^2 a^2), \quad (17)$$

where η_{het} is the heterodyne efficiency for detection of the ballistic light. In the experiments $a/a_o = 10$ and the heterodyne efficiency is found to be 0.4, which is due to difficulty in matching wave-front curvatures for beams of such disparate diameters. For the pedestal, only scattered light that is mode matched to the LO is detected. Thus the heterodyne efficiency for detection of the scattered light is 1.

With Eqs. (13) and (15), the smoothed Wigner distribution for the pedestal and the diffuse background normalized to S_{MBALL} is given by

$$\frac{S(x_M = 0, p_M)}{S_{\mathrm{MBALL}}} = A(\rho) F_P(p_\perp, \rho) + B \exp[-{p_\perp}^2/(\Delta p_B)^2]. \quad (18)$$

Here B is the amplitude, and Δp_B is the width of the broad background component that is fitted to the data. $A(\rho)$ is the magnitude of the pedestal mean square beat signal normalized to S_{MBALL}:

$$A(\rho) = \frac{\exp(-\mu_T L)}{\eta_{\mathrm{het}}^2 {\theta_o}^2 k^2 {a_o}^2} \int_0^\infty \mathrm{d}\eta_\perp \, 2\eta_\perp \times \{\exp[\mu_N L \exp(-{\eta_\perp}^2)] - 1\}. \quad (19)$$

$F_P(p_\perp)$ is the shape of the pedestal normalized to 1 at $p_\perp = 0$:

$$F_P(p_\perp) = \frac{W_P(x_\perp = 0, p_\perp)}{W_P(x_\perp = 0, p_\perp = 0)}, \quad (20)$$

where $W_P(x_\perp, p_\perp)$ is given by Eq. (13).

4. DISCUSSION

Equation (13) describes the Wigner phase-space distribution $W_P(x_\perp, p_\perp)$ for a pedestal that arises from multiple diffractive scattering. This pedestal has a much broader momentum distribution than the Wigner distribution for the ballistically transmitted field from which it arises.

Equation (13) has a simple physical interpretation. $W_P(x_\perp, p_\perp)$ can be expanded as a power series in $\mu_N L$ that explicitly displays the distributions for various numbers of multiple scatterings:

$$W_P(L, x_\perp, p_\perp) = \frac{\exp(-{x_\perp}^2/a^2)}{\pi a^2} \exp[-(\mu_T - \mu_N)L] \times \sum_{n=1}^{\infty} \exp(-\mu_N L) \times \frac{(\mu_N L)^n}{n!} \frac{\exp[-{p_\perp}^2/(n {\theta_o}^2 k^2)]}{\pi n {\theta_o}^2 k^2}. \quad (21)$$

Note that $x_\perp = \sqrt{x^2 + y^2}$ and similarly for $p_\perp$. For each term there is a normalized Gaussian momentum distribution of width $\theta_o k \sqrt{n}$ in the x and y directions. This describes a random-walk distribution for n momentum changes of magnitude $\theta_o k$. $\exp(-\mu_N L)(\mu_N L)^n/n!$ is a Poisson distribution describing the probability of n scatterings, where $\bar{n} = \mu_N L$ is the mean number of scattering events. With $\exp(-\mu_N L)$ incorporated into the probability of n scatterings, the pedestal decays as $\exp[-(\mu_T - \mu_N)L]$. The factor $\mu_B = \mu_T - \mu_N$ is just the extinction coefficient arising from large-angle scattering (and absorption).

Note that the missing $n = 0$ term in Eq. (21) that is nonzero for $\mu_N L = 0$ represents the ballistic contribution that was treated separately in determining the mean square beat signals of relation (3). Separation of these contributions is convenient, since the momentum distribution of the ballistically transmitted light is narrow compared with that of the LO beam whereas the momentum distribution for W_P is broad compared with that of the LO for the conditions of the experiment.

For $\mu_N L \gg 1$, W_P is approximately a single Gaussian distribution. In this case we can make the approximation

$$\exp[\mu_N L \exp(-{\eta_\perp}^2)] - 1 \simeq \exp[\mu_N L (1 - {\eta_\perp}^2)].$$

Here $\mu_N L \gg 1$ ensures that ${\eta_\perp}^2 \ll 1$ over the dominant region of integration. In this limit the Wigner distribution for the pedestal is given by

$$W_P(L, x_\perp, p_\perp) = \frac{\exp(-x^2/a^2)}{\pi a^2} \exp[-(\mu_T - \mu_N)L] \times \frac{\exp[-p^2/(\mu_N L {\theta_o}^2 k^2)]}{\pi \mu_N L {\theta_o}^2 k^2}. \quad (22)$$

Equation (22) describes a momentum distribution for a random walk with $\bar{n} = \mu_N L$ steps of size $\theta_o k$. This result arises because the width $\sqrt{\bar{n}}$ of the Poisson distribution of Eq. (21) is small compared with $\bar{n}$ for $\bar{n} \gg 1$. Hence the term in Eq. (21) with $n = \bar{n}$ dominates, yielding Eq. (22). Neglecting absorption, the pedestal decays as $\mu_T - \mu_N = \mu_B$, the extinction coefficient arising from large-angle scattering, as described above. Note that Eqs. (21) and (22) are valid only for small-angle scattering. Further, the input beam half-width at $1/e$ intensity, a, must be large enough so that $\theta_o \sqrt{\mu_N L} \ll a/L$. Hence there is negligible expansion of the input beam.

Theoretical Wigner phase-space distributions $S(x\mathrm{j} = 0, p)$ have been fitted to the data of Figs. 5–7 by using Eq. (18). The fits are shown as solid curves. The broad background is fitted by using the phenomenological con-

stants B and Δp_B and is not of interest here. However, the shape of the narrow pedestal is obtained from Eq. (20) by using the experimentally determined parameters: LO half-width at $1/e$ of $a_o = 0.38$ mm, half-width at $1/e$ for the input beam to the sample of $a = 3.8$ mm, and cell length $L = 1$ cm. The index of refraction of the background medium is $n_o = 1.36$. The optical wave vector in the medium is $k = n_o k_o$, where $k_o = 2\pi/\lambda_o$ is the wave vector in air, with $\lambda_o = 0.63\ \mu$m as the He–Ne laser wavelength. The heterodyne efficiency defined in Eq. (17) is $\eta_{\text{het}} = 0.4$. From the Mie solution (Fig. 2), we find that the half-width at $1/e$ of the central diffractive peak in the medium is $\theta_o = 23.2$ mrad. The total scattering cross section is $\sigma_S = 202\ \mu\text{m}^2$. The diffractive cross section σ_N is estimated from the area under the diffractive peak (for $0 \leqslant \theta \leqslant 0.1$ rad) to be $0.35\sigma_S$, and the remaining classical scattering cross section, obtained by integrating the differential cross section from $\theta = 0.1$ to π rad, is found to be $0.65\sigma_S$. The density ρ of scatterers is determined from the known volume fraction of the polystyrene spheres. Initially, the amplitude of the narrow pedestal, $A(\rho)$, is taken to be a free parameter that yields the best fits to the data. The figures show that very good fits are obtained.

Figure 8 shows the amplitude $A(\rho)$ obtained from the fits as a function of scatterer concentration ρ. Also shown is the prediction, based on Eq. (19). The prediction for the amplitude of the pedestal that arises from multiple diffractive scattering is found to be in very good agreement with the data using no free parameters.

For comparison, the decay of the ballistic signal with scatterer concentration is shown in Fig. 9. The ballistic signal decays exponentially according to $\exp(-\mu_S L)$, where $\mu_S = \rho\sigma_S$ as expected. By contrast, the pedestal arising from near-forward diffractive scattering decays much more slowly, as shown in Fig. 8. For concentrations beyond the maximum amplitude, this signal decays approximately exponentially with an attenuation coefficient $\mu_B = 0.65\mu_S$.

It is not difficult to understand why the diffractive pedestal decays more slowly than the ballistic signal. Diffractive momentum changes tend to scatter photons within the momentum distribution of the diffractive pedestal. Only large momentum changes are effective in scattering photons outside the momentum distribution of the pedestal. Hence the pedestal decays with the attenuation coefficient μ_B that arises from the large-angle scattering cross section. By contrast, both diffractive and large-angle momentum changes are effective in scattering photons out of the momentum distribution of the ballistic light, which is very narrow. Hence the ballistic distribution must decay with the extinction coefficient corresponding to the total scattering cross section μ_S.

5. CONCLUSIONS

In conclusion, we have demonstrated heterodyne measurement of smoothed Wigner phase-space distributions for light that has undergone multiple diffractive scattering in a turbid medium. This method provides high angular resolution and is well suited for direct measurement of momentum distributions in the near-forward scattering direction. The data are well fitted by a theoretical model that assumes that the Wigner phase-space distributions obey an approximate transport equation that is identical in structure to the usual transport equation for the specific intensity. By incorporating transverse momentum changes arising from multiple diffractive scattering and treating large-angle classical scattering as a loss, we find very good agreement with the data.

These experiments show that multiple diffractive scattering can produce a narrow pedestal that decays more slowly than the ballistically transmitted component. At high concentrations of scatterers, if the diffractive pedestal is comparable with the ballistic component, it can modify the apparent intensity of a probe beam compared with that expected for exponential attenuation of ballistic light. This is consistent with the anomalous probe intensity observed by Yadlowsky *et al.* in OCM.[19]

Our experiments are performed in a regime that is far outside the range where the diffusion approximation is valid. The diffusion limit has been investigated by Ishimaru *et al.*[29] In this work the position distribution is measured for the light emerging from a turbid medium containing small (either 0.1- or 2-μm) polystyrene spheres for different detector fields of view. In this case a narrow ballistic spatial peak and a broad diffuse background are obtained that agree well with calculations of the spatial distribution of the intensity based on the diffusion approximation. As the sphere size is increased, the differential scattering cross section becomes more forward peaked and the diffusion approximation breaks down, leading to disagreement with the data.

The language of Wigner distributions is well suited for rigorous description of the heterodyne measurement methods employed in our experiments. Wigner functions correctly incorporate coherent and incoherent contributions to the beat power spectrum, including both ballistic and scattered light. The good agreement between the data and the model shows that approximating the transport equation for the Wigner distribution by the usual radiative transport equation is appropriate for the conditions of the experiments. Since the approximate analysis presented here is equivalent to that based on the radiative transport equation for the specific intensity, it is similar to that presented in previous studies of small-angle scattering.[28] However, we expect that when the Wigner distribution in the medium varies substantially over optical wavelength scales, the appropriate transport equation may be nonlocal, and the simple approximations used in this work may break down.[4]

Previously, smoothed Wigner distributions have been identified with the specific intensity of radiative transport theory.[4,30] However, it is important to distinguish the propagation of smoothed Wigner distributions in the medium from smoothing of the output Wigner distribution by the measurement method, as in our heterodyne detection scheme. In cases where the radiative transport equation breaks down, the transport equation for the true Wigner distribution may still be needed to correctly determine the output Wigner distribution that is smoothed in the measurements.

The heterodyne method for measurement of Wigner

distributions has a high dynamic range and can be used to study transmitted and reflected light in dense turbid media. Although the present work concentrated on the momentum, the joint evolution of the position and momentum distribution can be studied by this method. In the present experiments, which employ cw lasers, the small-angle scattering distributions are overwhelmed by the diffuse background as the concentration of scatterers is increased. Hence the decay of the pedestal arising from multiple diffractive scattering could not be studied at very high concentrations with correspondingly high dynamic range. However, if similar experiments with a low-coherence light source are performed, diffuse scatter can be substantially suppressed and the evolution of the diffractive pedestal can be followed to much higher scatterer concentrations. Experiments employing this method to measure Wigner distributions for low-order scattered light are currently under way in our laboratory.

APPENDIX A: WIGNER DISTRIBUTION FOR SMALL-ANGLE SCATTERING

In this appendix we determine the Wigner distribution for small-angle scattering under the conditions of the experiments.

As discussed in Section 3, in the simplest approximation, the Wigner distribution obeys a transport equation identical in structure to the usual radiative transport equation for the specific intensity[31]:

$$\frac{c^2\mathbf{p}}{{n_o}^2\omega}\cdot\nabla_x W(\mathbf{x},\mathbf{p}) = -\frac{c}{n_o}\mu_T(\mathbf{p})W(\mathbf{x},\mathbf{p}) + \int \mathrm{d}^3\mathbf{p}'\,K(\mathbf{p},\mathbf{p}')W(\mathbf{x},\mathbf{p}'). \tag{A1}$$

Here the scattering kernel $K(\mathbf{p},\mathbf{p}')$ takes the approximate form

$$K(\mathbf{p},\mathbf{p}') = \rho\frac{c^2}{{n_o}^2\omega}\,\delta\left(\frac{\mathbf{p}^2-\mathbf{p}'^2}{2}\right)|f(\mathbf{p},\mathbf{p}')|^2, \tag{A2}$$

where $f(\mathbf{p},\mathbf{p}')$ is the scattering amplitude. Note that

$$\int \mathrm{d}^3\mathbf{p}'\,K(\mathbf{p},\mathbf{p}') = \frac{c}{n_o}\mu_s(\mathbf{p}) \tag{A3}$$

is the total scattering rate, including both large- and small-angle scattering.

As discussed in Subsection 3.A, we assume that the kernel consists of two components, a narrow diffractive component K_N and a broad classical scattering component K_B:

$$K(\mathbf{p},\mathbf{p}') = K_N(\mathbf{p},\mathbf{p}') + K_B(\mathbf{p},\mathbf{p}'). \tag{A4}$$

We further assume that the Wigner distribution can be decomposed into three components:

$$W(\mathbf{x},\mathbf{p}) = W_{\mathrm{BALL}}(\mathbf{x},\mathbf{p}) + W_P(\mathbf{x},\mathbf{p}) + W_B(\mathbf{x},\mathbf{p}). \tag{A5}$$

Here BALL denotes the narrow ballistic component, P denotes the narrow pedestal arising from multiple diffractive scattering, and B denotes the broad background.

The ballistic contribution has a very narrow momentum distribution compared with the width of both K_N and K_B. Hence the integral term in Eq. (A1) can be neglected in its propagation, and W_{BALL} obeys the equation

$$\frac{c\mathbf{p}}{n_o k}\cdot\nabla_x W_{\mathrm{BALL}}(\mathbf{x},\mathbf{p}) = -\frac{c}{n_o}\mu_T W_{\mathrm{BALL}}(\mathbf{x},\mathbf{p}). \tag{A6}$$

Using Eqs. (A4)–(A6) in Eq. (A1) yields an equation for the narrow pedestal arising from small-angle scattering:

$$\frac{c\mathbf{p}}{n_o k}\cdot\nabla_x W_P(\mathbf{x},\mathbf{p}) = -\frac{c}{n_o}\mu_T W_P(\mathbf{x},\mathbf{p}) + \int \mathrm{d}^3\mathbf{p}'\,K_N(\mathbf{p},\mathbf{p}')W_P(\mathbf{x},\mathbf{p}') + \int \mathrm{d}^3\mathbf{p}'\,K_N(\mathbf{p},\mathbf{p}')W_{\mathrm{BALL}}(\mathbf{x},\mathbf{p}'). \tag{A7}$$

The last term on the right-hand side of Eq. (A7) arises from small-angle scattering of the ballistic phase-space distribution. It acts as the source for the pedestal. The first integral term on the right-hand side describes multiple scattering of the phase-space distribution of the pedestal. This equation can be straightforwardly solved by Green's-function methods as shown below.

Similarly, the broad phase-space component obeys the equation

$$\frac{c\mathbf{p}}{n_o k}\cdot\nabla_x W_B(\mathbf{x},\mathbf{p}) = -\frac{c}{n_o}\mu_T W_B(\mathbf{x},\mathbf{p}) + \int \mathrm{d}^3\mathbf{p}'[K_N(\mathbf{p},\mathbf{p}') + K_B(\mathbf{p},\mathbf{p}')]W_B(\mathbf{x},\mathbf{p}') + \int \mathrm{d}^3\mathbf{p}'\,K_B(\mathbf{p},\mathbf{p}')[W_{\mathrm{BALL}}(\mathbf{x},\mathbf{p}') + W_P(\mathbf{x},\mathbf{p}')]. \tag{A8}$$

The first integral term on the right-hand side of Eq. (A8) contains the large-angle scattering kernel that causes multiple scattering of the broad phase-space distribution. The narrow kernel causes scattering within W_B and does not cause attenuation of W_B. In this case the decay rate of W_B is approximately $(c/n_o)\mu_T - \int \mathrm{d}^3\mathbf{p}'\,K(\mathbf{p},\mathbf{p}')$. Large-angle scattering of the ballistic and narrow pedestal distributions acts as the source for the broad component of the phase-space distribution. The sum of Eqs. (A6)–(A8) reproduces Eq. (7) with the two-component kernel. Equation (A8) will not be needed, as our interest is in the phase-space distribution for the narrow pedestal, W_P.

To model the small-angle scattering data, we assume that large-angle scattering introduces loss for the phase-space distribution of the pedestal, whereas diffractive scattering causes small-angle momentum changes. In this case the **z** component of momentum is approximately constant. The diffractive component of the Mie scatter-

ing solution is approximately Gaussian in shape and yields a differential cross section of the form

$$|f(\mathbf{p},\,\mathbf{p}')|^2 = \frac{d\sigma}{d\Omega} = \frac{\sigma_N}{\pi\theta_o{}^2}\exp\left[-\frac{(\Delta\mathbf{p}_\perp)^2}{\theta_o{}^2p^2}\right]. \tag{A9}$$

Here σ_N is the cross section for diffractive scattering, θ_o is the scattering diffraction angle, of order $\theta_o \simeq 2/(ka_S)$, where a_S is the radius of the scatterer, and $p = k = n_o\omega/c$ is the wave vector in the medium. The scattering angle is $\theta = |\Delta\mathbf{p}_\perp|/p$, where $\Delta\mathbf{p}_\perp = \mathbf{p}_\perp - \mathbf{p}'_\perp$ is the momentum change transverse to the $\mathbf{z}$ direction. The differential cross section is normalized so that

$$\int d\Omega\,\frac{d\sigma}{d\Omega} \simeq \int_0^\infty 2\pi\theta\,d\theta\,\frac{\sigma_N}{\pi\theta_o{}^2}\exp\left(-\frac{\theta^2}{\theta_o{}^2}\right) = \sigma_N.$$

Using Eq. (A9), we can simplify the collision kernel [Eq. (A2)] for small-angle scattering. With $\delta(\mathbf{p}^2/2 - \mathbf{p}'^2/2) = \delta(p - p')/k \simeq \delta(p_z - p'_z)/k$, the collision kernel K_N takes the approximate form

$$K_N(\mathbf{p},\,\mathbf{p}') \simeq K_N(\mathbf{p}-\mathbf{p}') = \frac{c}{n_o}\mu_N\delta(p_z - p'_z)\,\frac{1}{\pi\theta_o{}^2k^2} \times \exp\left[-\frac{(\Delta\mathbf{p}_\perp)^2}{\theta_o{}^2p^2}\right], \tag{A10}$$

where $\mu_N = \rho\sigma_N$ is the attenuation coefficient for diffractive scattering. The diffractive kernel is normalized so that

$$\int d^3\Delta\mathbf{p}\,K_N(\Delta\mathbf{p}) = \Gamma_N = \frac{c}{n_o}\mu_N, \tag{A11}$$

where Γ_N is the diffractive scattering rate.

Equation (A7) is readily solved by using a Green's-function method with the approximations that the total scattering rate is independent of momentum and the kernel is a function of $\mathbf{p} - \mathbf{p}'$ only. In this case the Green's function G_p satisfies

$$\left(\frac{c\mathbf{p}}{n_ok}\cdot\nabla_x + \Gamma_T\right)G_p(\mathbf{x},\,\mathbf{x}';\mathbf{p},\,\mathbf{p}') - \int d^3\mathbf{p}''\,K(\mathbf{p}-\mathbf{p}') \times G_p(\mathbf{x},\,\mathbf{x}';\mathbf{p}'',\,\mathbf{p}') = \delta(\mathbf{x}-\mathbf{x}')\delta(\mathbf{p}-\mathbf{p}'). \tag{A12}$$

Here the total loss rate is

$$\Gamma_T = (c/n_o)\mu_T. \tag{A13}$$

The Green's function is easily obtained by Fourier transform methods[31] and is given by

$$G_p(\mathbf{x},\,\mathbf{x}';\mathbf{p},\,\mathbf{p}') = \int\frac{d^3\mathbf{q}}{(2\pi)^3}\int\frac{d^3\mathbf{r}}{(2\pi)^3} \times \exp[i\mathbf{q}\cdot(\mathbf{x}-\mathbf{x}') + i\mathbf{r}\cdot(\mathbf{p}-\mathbf{p}')] \times n_o/c\int_0^\infty dl\,\exp(-il\mathbf{q}\cdot\mathbf{p}'/k) \times \exp\left[-\int_0^l dl'\,\tilde{\mu}(\mathbf{r}+\mathbf{q}l'/k)\right], \tag{A14}$$

where $k = n_o\omega/c$ is the magnitude of the optical wave vector. Here

$$\frac{c}{n_o}\tilde{\mu}(\mathbf{r}) \equiv \frac{c}{n_o}\mu_T - \tilde{K}(\mathbf{r}), \tag{A15}$$

where

$$\tilde{K}(\mathbf{r}) = \int d^3\Delta\mathbf{p}\,\exp(-i\Delta\mathbf{p})K(\Delta\mathbf{p}). \tag{A16}$$

With relation (10) for the ballistic component, the source term for the phase-space distribution of the narrow pedestal in Eq. (A7) is given by

$$S(\mathbf{x},\,\mathbf{p}) = \int d^3\mathbf{p}'\,K_N(\mathbf{p},\,\mathbf{p}')W_{\mathrm{BALL}}(\mathbf{x},\,\mathbf{p}'). \tag{A17}$$

With use of the Green's function [Eq. (A14)], the phase-space distribution for the narrow pedestal of Eq. (A7) is given by

$$W_P(\mathbf{x},\,\mathbf{p}) = \int d^3\mathbf{x}'d^3\mathbf{p}'G_p(\mathbf{x},\,\mathbf{x}';\mathbf{p},\,\mathbf{p}')S(\mathbf{x}',\,\mathbf{p}'). \tag{A18}$$

With the approximate kernel of relation (A10), the Green's function [Eq. (A14)] is determined by using $\tilde{\mu}(\mathbf{r})$ [Eq. (A15)]. In this case $\tilde{\mu}(\mathbf{r})$ is independent of r_z, so that

$$\tilde{\mu}(\mathbf{r}_\perp) = \mu_T - \mu_N\exp\left[-\frac{\theta_o{}^2k^2}{4}(r_x{}^2 + r_y{}^2)\right] \equiv \mu_T - \tilde{K}'(\mathbf{r}_\perp). \tag{A19}$$

The source for the narrow pedestal, $S(\mathbf{x},\,\mathbf{p})$ [Eq. (A17)], is

$$S(\mathbf{x},\,\mathbf{p}) = \frac{c}{n_o}\mu_N\frac{\exp(-\mu_Tz)}{\pi a^2}\exp\left(-\frac{x^2+y^2}{a^2}\right)\frac{\delta(p_z-k)}{\pi\theta_o{}^2k^2} \times \exp\left(-\frac{p_x{}^2+p_y{}^2}{\theta_o{}^2k^2}\right). \tag{A20}$$

Here we have assumed that the input field $1/e$ radius, a, is sufficiently large that the diffraction angle of the input field, $2/(ka)$, satisfies $2/(ka) \ll \theta_o$, as is the case in our experiments. Note that the source is nonzero only in the medium, so that $0 \leq z \leq L$, where $z = L$ is the output face of the sample.

The phase-space distribution for the pedestal, W_P, is now easily determined from Eq. (A18). Since $\tilde{\mu}(\mathbf{r}_\perp)$ [Eq. (A19)] is independent of r_z, the r_z and q_z integrals in the Green's function [Eq. (A14)] are readily carried out and yield delta functions $\delta(p_z - p'_z)$ and $\delta[l - (z$

$- z')k/p_z']$. With the source function [Eq. (A20)], $p_z' = k$, so that $l = z - z' = L - z'$ for $z = L$. With the use of Eqs. (A16) and (A19) for $\tilde{K}'(\mathbf{r}_\perp)$, it is straightforward to obtain

$$W_P(L, \mathbf{x}_\perp; \mathbf{p}) = \delta(p_z - k)\exp(-\mu_T L) \times \int \frac{d^2\mathbf{q}_\perp}{(2\pi)^2} \exp(i\mathbf{q}_\perp \cdot \mathbf{x}_\perp) \times \int \frac{d^2\mathbf{r}_\perp}{(2\pi)^2} \exp(i\mathbf{r}_\perp \cdot \mathbf{p}_\perp - a^2\mathbf{q}_\perp{}^2/4) \times \int_0^L dz'\, \tilde{K}'[\mathbf{r}_\perp + (L - z')\mathbf{q}_\perp/k] \times \exp\left[\int_0^{L-z'} dl'\, \tilde{K}'(\mathbf{r}_\perp + \mathbf{q}_\perp l'/k)\right]. \quad \text{(A21)}$$

The z' integral in Eq. (A21) is just

$$\exp\left[\int_0^L dl'\, \tilde{K}'(\mathbf{r}_\perp + \mathbf{q}_\perp l'/k)\right] - 1.$$

Hence the phase-space density W_P is given by

$$W_P(L, \mathbf{x}_\perp; \mathbf{p}) = \delta(p_z - k)\exp(-\mu_T L) \times \int \frac{d^2\mathbf{q}_\perp}{(2\pi)^2} \exp(i\mathbf{q}_\perp \cdot \mathbf{x}_\perp - a^2\mathbf{q}_\perp{}^2/4) \times \int \frac{d^2\mathbf{r}_\perp}{(2\pi)^2} \exp(i\mathbf{r}_\perp \cdot \mathbf{p}_\perp) \times \left\{\exp\left[\int_0^L dl'\, \tilde{K}'(\mathbf{r}_\perp + \mathbf{q}_\perp l'/k)\right] - 1\right\}. \quad \text{(A22)}$$

It is convenient to define the transverse phase-space distribution $W_P(L, \mathbf{x}_\perp, \mathbf{p}_\perp)$ by

$$W_P(L, \mathbf{x}_\perp; \mathbf{p}) = \delta(p_z - k) W_P(L, \mathbf{x}_\perp, \mathbf{p}_\perp). \quad \text{(A23)}$$

To check the normalization of $W_P(L, \mathbf{x}_\perp, \mathbf{p}_\perp)$, note that integrating Eq. (A22) over $\mathbf{x}_\perp$ and $\mathbf{p}_\perp$ yields delta functions in $\mathbf{q}_\perp$ and $\mathbf{r}_\perp$. Using $\tilde{K}'(0) = \mu_N$, which follows from Eq. (A19), one then obtains

$$\int d^2\mathbf{x}_\perp \int d^2\mathbf{p}_\perp\, W(L, \mathbf{x}_\perp, \mathbf{p}_\perp) = \exp(-\mu_T L)[\exp(\mu_N L) - 1] = \exp(-\mu_B L) - \exp(-\mu_T L). \quad \text{(A24)}$$

Here $\mu_B \equiv \mu_T - \mu_N$ is the attenuation coefficient arising from large-angle scattering and absorption, i.e., the minimum attenuation rate for the pedestal phase-space distribution. This attenuation rate occurs when the pedestal is broad in transverse momentum compared with the diffractive kernel but narrow compared with the large-angle scattering kernel. In this case large-angle collisions and absorption are effective in attenuating W_P, but diffractive collisions are ineffective, as they cause scattering *within* the distribution. The source of the pedestal is just the diffractive scattering probability $\mu_N\, dz'$ times the intensity of the ballistic component, $\exp(-\mu_T z')$. The pedestal contribution decays as $\exp[-\mu_B(L - z')]$. Hence one expects an integrated output intensity given by

$$\int_0^L dz'\, \mu_N \exp(-\mu_T L)\exp[-\mu_B(L - z')] = \exp(-\mu_B L) - \exp(-\mu_T L),$$

in agreement with Eq. (A24).

When the input field $1/e$ radius a is sufficiently large that $a/L \gg \theta_o$, Eq. (A22) can be further simplified. Note that $q_\perp \simeq 1/a$ and l' is at most L in the argument of $\tilde{K}'$. Then the maximum value of $q_\perp l'/k$ is $L/(ka)$. The maximum value of $r_\perp$ is of order $2/(k\theta_o)$, since $\tilde{K}' \to 0$ if $r_\perp > 2/(k\theta_o)$. If $a/L \gg \theta_o$, the $\mathbf{q}_\perp$ dependence in the argument of $\tilde{K}'$ can be neglected and the $\mathbf{q}_\perp$ integral performed to obtain a Gaussian spatial distribution identical to that of the input field. This is consistent with the assumption of a being large enough to achieve approximate translation invariance. The phase-space distribution for the pedestal then takes the simple form

$$W_P(L, \mathbf{x}_\perp, \mathbf{p}_\perp) = \frac{\exp(-\mathbf{x}_\perp{}^2/a^2)}{\pi a^2} \exp(-\mu_T L) \times \int \frac{d^2\mathbf{r}_\perp}{(2\pi)^2} \exp(i\mathbf{r}_\perp \cdot \mathbf{p}_\perp) \times \left\{\exp\left[\mu_N L \exp\left(-\frac{\theta_o{}^2 k^2 \mathbf{r}_\perp{}^2}{4}\right)\right] - 1\right\}. \quad \text{(A25)}$$

In the limit $\mu_N L \gg 1$, the Gaussian in the exponent appearing in Eq. (A25) can be expanded to lowest order in $\mathbf{r}_\perp{}^2$ to give a Gaussian function of $r_\perp$ for which the $1/e$ width is of order $2(\theta_o k\sqrt{\mu_N L})^{-1}$. In this limit multiple diffractive scattering causes momentum diffusion. As long as $(a/L)^2 \gg \mu_N L(\theta_o k/2)^2$, i.e., the mean square width of the momentum distribution for $\mu_N L$ scatterings is smaller than the mean square angular aperture of the illuminated volume, the approximations used to obtain Eq. (A25) remain valid.

The $\mathbf{r}_\perp$ integral in Eq. (A25) can be simplified by introducing the dimensionless variable $\eta_\perp \equiv \theta_o k\mathbf{r}_\perp/2$. Using $\eta_\perp \cdot \mathbf{p}_\perp = \eta_\perp p_\perp \cos\phi$ and $d^2\eta_\perp = \eta_\perp\, d\eta_\perp d\phi$, we have

$$\int_0^{2\pi} \frac{d\phi}{2\pi} \exp\left(i\,\frac{2p_\perp}{\theta_o k}\,\eta_\perp \cos\phi\right) = J_0\left(\eta_\perp \frac{2p_\perp}{\theta_o k}\right).$$

Then the transverse Wigner distribution for the pedestal is given by

$$W_P(L, x_\perp, p_\perp) = \frac{\exp(-x_\perp{}^2/a^2)}{\pi^2\theta_o{}^2 k^2 a^2} \exp(-\mu_T L) \times \int_0^\infty d\eta_\perp\, 2\eta_\perp J_0\left(\eta_\perp \frac{2p_\perp}{\theta_o k}\right) \times \{\exp[\mu_N L \exp(-\eta_\perp{}^2)] - 1\}. \quad \text{(A26)}$$

Here the transverse position is $x_\perp = \sqrt{x^2 + y^2}$, and similarly for the transverse momentum $p_\perp$. The normalization of Eq. (A26) is identical to that of Eq. (A24), as is readily shown by using

$$\int d^2\mathbf{p}_\perp \, J_0\left(\eta_\perp \frac{2p_\perp}{\theta_o k}\right) = \frac{\pi}{2}\,\theta_o{}^2 k^2 \,\frac{\delta(\eta_\perp)}{\eta_\perp}.$$

ACKNOWLEDGMENTS

This research has been supported by the National Institutes of Health and the National Science Foundation. We thank R. Glauber for suggesting experiments in the regime used for the measurements and M. G. Raymer for many stimulating discussions regarding Wigner distributions.

The authors can be reached at the address on the title page, by telephone at 919-660-2508, or by e-mail at jet@phy.duke.edu.

REFERENCES AND NOTES

1. A. Yodh and B. Chance, "Spectroscopy and imaging with diffusing light," Phys. Today **48**(3), 34–40 (1995).
2. M. G. Raymer, C. Cheng, D. M. Toloudis, M. Anderson, and M. Beck, "Propagation of Wigner coherence functions in multiple scattering media," in *Advances in Optical Imaging and Photon Migration*, R. R. Alfano and J. G. Fujimoto, eds., Vol. 2 of OSA Trends in Optics and Photonics Series (Optical Society of America, Washington, D.C., 1996), pp. 236–238.
3. D. F. McAlister, M. Beck, L. Clarke, A. Mayer, and M. G. Raymer, "Optical phase retrieval by phase-space tomography and fractional-order Fourier transforms," Opt. Lett. **20**, 1181–1183 (1995).
4. S. John, G. Pang, and Y. Yang, "Optical coherence propagation and imaging in a multiple scattering medium," J. Biomed. Opt. **1**, 180–191 (1996).
5. E. P. Wigner, "On the quantum correction for thermodynamic equilibrium," Phys. Rev. **40**, 749–759 (1932).
6. M. Hillery, R. F. O'Connel, M. O. Scully, and E. P. Wigner, "Distribution functions in physics: fundamentals," Phys. Rep. **106**, 121–167 (1984).
7. D. Huang, E. A. Swanson, C. P. Lin, J. S. Schuman, C. A. Puliafito, and J. G. Fujimoto, "Optical coherence tomography," Science **254**, 1178–1181 (1991).
8. J. A. Izatt, M. D. Kulkerni, K. Kobayashi, M. S. Sivak, J. K. Barton, and A. J. Welch, "Optical coherence tomography for biodiagnostics," Opt. Photon. News **8**(5), 41–47, 65 (1997).
9. J. A. Izatt, M. R. Hee, G. M. Owen, E. A. Swanson, and J. G. Fujimoto, "Optical coherence microscopy in scattering media," Opt. Lett. **19**, 590–592 (1994).
10. D. A. de Wolf and J.-K. Pack, "Wave-kinetic numerical approach to propagation of optical beams," J. Opt. Soc. Am. A **3**, 532–535 (1986); J.-K. Pack and D. A. de Wolf, "Wave-kinetic numerical approach to propagation of optical beams. II. Two canonical problems," J. Opt. Soc. Am. A **3**, 1766–1771 (1986).
11. For a review see M. J. Bastiaans, "Application of the Wigner distribution function to partially coherent light," J. Opt. Soc. Am. A **3**, 1227–1238 (1986).
12. C. Iaconis and I. A. Walmsley, "Direct measurement of the two-point field correlation function," Opt. Lett. **21**, 1783–1785 (1996).
13. A. Wax and J. E. Thomas, "Optical heterodyne imaging and Wigner phase space distributions," Opt. Lett. **21**, 1427–1429 (1996).
14. A. Wax and J. E. Thomas, "Heterodyne measurement of Wigner phase space distributions in turbid media," in *Advances in Optical Imaging and Photon Migration*, R. R. Alfano and J. G. Fujimoto, eds., Vol. 2 of OSA Trends in Optics and Photonics Series (Optical Society of America, Washington, D.C., 1996), pp. 238–242.
15. M. Beck, M. E. Anderson, and M. Raymer, "Imaging through scattering media using pulsed homodyne detection," in *Advances in Optical Imaging and Photon Migration*, R. R. Alfano, ed., Vol. 21 of OSA Proceedings Series (Optical Society of America, Washington, D.C., 1994), pp. 257–260.
16. A. Schmidt, R. Corey, and P. Saulnier, "Imaging through random media by use of low-coherence optical heterodyning," Opt. Lett. **20**, 404–406 (1995).
17. A. Ya. Polishchuk and R. R. Alfano, "Fermat photons in turbid media: an exact analytic solution for most favorable paths—a step toward optical tomography," Opt. Lett. **20**, 1937–1939 (1995).
18. L. T. Perelman, J. Wu, I. Itzkan, and M. S. Feld, "Photon migration in turbid media using path integrals," Phys. Rev. Lett. **72**, 1341–1344 (1994); L. T. Perelman, J. Wu, I. Itzkan, Y. Wang, R. R. Dasari, and M. S. Feld, "Photon paths in turbid media: theory and experimental observation," in *Advances in Optical Imaging and Photon Migration*, R. R. Alfano, ed., Vol. 21 of OSA Proceedings Series (Optical Society of America, Washington, D.C., 1994), pp. 153–155.
19. M. J. Yadlowsky, J. M. Schmidt, and R. F. Bonner, "Multiple scattering in optical coherence microscopy," Appl. Opt. **34**, 5699–5707 (1995).
20. The mean square beat is positive definite and takes the form of a smoothed Wigner distribution. See N. D. Cartwright, "A non-negative Wigner-type distribution," Physica (Utrecht) **83A**, 210–212 (1976).
21. H. P. Yuen and V. W. S. Chan, "Noise in homodyne and heterodyne detection," Opt. Lett. **8**, 177–179 (1983).
22. This method has been used in light beating spectroscopy. See H. Z. Cummins and H. L. Swinney, "Light beating spectroscopy," in *Progress in Optics VIII*, E. Wolf, ed. (North-Holland, New York, 1970), Chap. 3, pp. 133–200.
23. This method has been used by G. L. Abbas, V. W. S. Chan, and T. K. Yee, "A dual detector optical heterodyne receiver for local oscillator noise suppression," J. Lightwave Technol. **3**, 1110–1112 (1985).
24. See, for example, V. J. Corcoran, "Directional characteristics in optical heterodyne detection processes," J. Appl. Phys. **36**, 1819–1825 (1965); A. E. Siegman, "The antenna properties of optical heterodyne receivers," Appl. Opt. **5**, 1588–1594 (1966); S. Cohen, "Heterodyne detection: phase front alignment, beam spot size, and detector uniformity," Appl. Opt. **14**, 1953–1959 (1975); A. L. Migdall, B. Roop, Y. C. Zheng, J. E. Hardis, and Gu Jun Xia, "Use of heterodyne detection to measure optical transmittance over a wide range," Appl. Opt. **29**, 5136–5144 (1990).
25. C. F. Bohren and D. R. Huffman, *Absorption and Scattering of Light by Small Particles* (Wiley-Interscience, New York, 1983).
26. The idea of making measurements of Wigner distributions in this regime was suggested to us by R. J. Glauber, Department of Physics, Harvard University, Cambridge, Massachusetts 02138 (personal communication, May 1996).
27. Yu. N. Barabanenkov, "On the spectral theory of radiation transport equations," Sov. Phys. JETP **29**, 679–684 (1969).
28. A. Zardecki and S. A. W. Gerstl, "Multi-Gaussian phase function model for off-axis laser beam scattering," Appl. Opt. **26**, 3000–3004 (1987).
29. A. Ishimaru, Y. Kuga, R. Cheung, and K. Shimizu, "Scattering and diffusion of a beam wave in randomly distributed scatterers," J. Opt. Soc. Am. **73**, 131–136 (1983).
30. J. Cooper and P. Zoller, "Radiative transfer equations in broad-band, time-varying fields," Astrophys. J. **277**, 813–819 (1984).
31. See, for example, A. Ishimaru, *Wave Propagation and Scattering in Random Media* (Academic, New York, 1978), Vols. I and II.